Monthly Notices of the ROYAL ASTRONOMICAL SOCIETY

MNRAS **507,** 548–559 (2021) https://doi.org/10.1093/mnras/stab2196
Advance Access publication 2021 July 31

The origin of the dust extinction curve in milky way-like galaxies

Qi Li [1]★ Desika Narayanan [1,2] Paul Torrey [1] Romeel Davé [3,4,5] and Mark Vogelsberger [6]

[1]*Department of Astronomy, University of Florida, 211 Bryant Space Science Center, Gainesville, FL 32611, USA*
[2]*Cosmic Dawn Center (DAWN), Niels Bohr Institute, University of Copenhagen, Juliane Maries vej 30, DK-2100 Copenhagen, Denmark*
[3]*Institute for Astronomy, Royal Observatory, Edinburgh EH9 3HJ, UK*
[4]*University of the Western Cape, Bellville, Cape Town 7535, South Africa*
[5]*South African Astronomical Observatory, Cape Town 7925, South Africa*
[6]*Department of Physics, Kavli Institute for Astrophysics and Space Research, Massachusetts Institute of Technology, Cambridge, MA 02139, USA*

Accepted 2021 July 24. Received 2021 July 23; in original form 2020 December 9

ABSTRACT

We develop a cosmological model for the evolution of dust grains in galaxies with a distribution of sizes in order to understand the origin of the Milky Way dust extinction curve. Our model considers the formation of active dust in evolved stars, growth by accretion and coagulation, and destruction processes via shattering, sputtering, and astration in the ISM of galaxies over cosmic time. Our main results follow. Galaxies in our cosmological model with masses comparable to the Milky Way's at $z \sim 0$ exhibit a diverse range of extinction laws, though with slopes and bump strengths comparable to the range observed in the Galaxy. The progenitors of the Milky Way have steeper slopes, and only flatten to slopes comparable to the Galaxy at $z \sim 1$. This owes to increased grain growth rates at late times/in high-metallicity environments driving up the ratio of large to small grains, with a secondary dependence on the graphite-to-silicate ratio evolution. The UV bump strengths depend primarily on the graphite-to-silicate ratio, and remain broadly constant in MW-like galaxies between $z = 3$ and $z = 0$, though show slight variability. Our models span comparable regions of bump-slope space as sightlines in the Galaxy do, though there is a lack of clear relationship between the model slopes and bump strengths owing to variations among galaxies in the graphite-to-silicate ratio. Our model provides a novel framework to study the origins and variations of dust extinction curves in galaxies over cosmic time.

Key words: (ISM:) dust, extinction – galaxies: evolution – galaxies: ISM.

1 INTRODUCTION

The extinction of photons by dust in the interstellar medium (ISM) of galaxies is the amount of radiation lost on an individual sightline owing to either absorption or scattering away from the line of sight (see the recent reviews by Galliano, Galametz & Jones 2018 and Salim & Narayanan 2020).[1] Generally, the wavelength-dependent nature of extinction is characterized by a family of curves or 'laws' that rise towards shorter wavelengths, with a bump in extinction near 2175 Å that is often referred to as the UV bump (Stecher & Donn 1965). Quantifying the shape and normalization of extinction laws is critical for de-reddening UV-to-near-infrared observations to properly estimate physical quantities such as star formation rates and stellar masses. Generally, the extinction law represents a weighted mean of the wavelength dependence of the extinction cross-section by the dust grain size distribution in the ISM.

The best observational constraints of extinction curves come from nearby sources, owing to the need for well-resolved sightlines. A fundamental requirement for these measurements is a priori knowledge of the shape of the unreddened spectra or spectral energy distribution (SED). In the Milky Way, the most common method is to use what is known as the pair method: here, the SED of an observed star is compared against one that is dust-free, and of a similar spectral type (Stebbins, Huffer & Whitford 1939; Stecher & Donn 1965; Fitzpatrick & Massa 1986), though some studies have instead employed theoretical stellar atmosphere models as the dust-free references (Fitzpatrick & Massa 2007).

More recently, a number of studies have employed large-survey statistical approaches to deriving extinction laws. As an example, Peek & Graves (2010) developed a method monikered 'standard crayons' which used passive galaxies as standard background sources to measure the reddening at high Galactic latitudes. This method was expanded by Berry et al. (2012) and Schlafly et al. (2014, 2016), who used SED fitting to derive the intrinsic SEDs of stars from the large-scale surveys (e.g. Sloan digital Sky Survey (SDSS), Two-Micron All Sky Survey (2MASS), Pan-STARRS1, and APOGEE). Other large-scale surveys to map the dust extinction law in the Galaxy include Schlafly et al. (2010), Schlafly & Finkbeiner (2011), and Wang & Chen (2019).

The seminal studies by Fitzpatrick & Massa (1988) and Cardelli, Clayton & Mathis (1989) computed the extinction law within the Milky Way over tens of individual sightlines, and determined that even within an individual galaxy there is substantial dispersion in

★ E-mail: pg3552@ufl.edu

[1]This is to be distinguished by 'attenuation' which quantifies the net loss of light from many unresolved sightlines, and therefore includes the impact of both scattering back into the line of sight, as well as the contribution to the observed signal by unobscured stars.

both the slopes and UV bump strength of the curves. Cardelli et al. further inferred that the slopes of these curves between the *V*-band and UV wavelengths were correlated with $R_V^{-1} \equiv (A_B/A_V - 1)$, though the scatter is significant. In this paper, we will regularly compare to both the range of curves observed by Cardelli et al. (1989), as well as the average Fitzpatrick & Massa (2007) curve.

While the extinction law in the Galaxy may follow a self-similar family of curves (though this is unclear; Salim & Narayanan 2020), this does not extend to the Magellanic clouds, which demonstrate (on average) as a function of decreasing metallicity, steeper slopes with reduced UV bump strengths (Clayton & Martin 1985; Fitzpatrick 1985). While, like the Galaxy, significant sightline-dependent variation exists (e.g. Prevot et al. 1984; Pei 1992; Gordon & Clayton 1998; Gordon et al. 2003), on average, the LMC is steeper than the Milky Way, and the SMC is steeper yet. Outside of the Galaxy and Clouds, extinction law constraints in M31 (Dong et al. 2014), and galaxies outside of the Local Group (using back lights such as other galaxies, GRBs or quasars; White & Keel 1992; York et al. 2006; Stratta et al. 2007; Holwerda et al. 2009; Zafar et al. 2011, 2018) have demonstrated strong variations in both their slopes and 2175 Å UV bump strengths. The origin of variations in extinction law slopes and bump strengths in galaxies is currently unknown, and an area in which theoretical models can provide some insight.

Broadly, models for extinction curves fall into two categories: synthesis and numerical (see Salim & Narayanan 2020 for a review). In the former category, the goal is to develop a theory that simultaneously models the grain size distribution and composition of dust in the face of numerous observational constraints that include (but are not limited to) the observed wavelength-dependent extinction curve, polarization signatures, and broad-band infrared emission features. Mathis, Rumpl & Nordsieck (1977) (hereafter, MRN) developed a seminal model in which they found a power-law size distribution and combination of graphite-silicate grains performed well in fitting the existing Galactic extinction constraints (this model was subsequently expanded on substantially by Draine & Lee 1984 and Laor & Draine 1993). Other groups have departed either from the canonical MRN power-law size distributions (e.g. lognormals) in order to explain various features of the Galactic extinction curve (e.g. Kim, Martin & Hendry 1994; Li & Draine 2001), or employed non-purely graphite-silicate dust compositions (motivated in large part by observed emission from polycyclic aromatic hydrocarbons; Jones, Duley & Williams 1990; Siebenmorgen & Kruegel 1992; Dwek et al. 1997; Li & Greenberg 1997; Weingartner & Draine 2001; Zubko, Dwek & Arendt 2004; Galliano et al. 2011; Jones et al. 2017).

The second major class of theoretical models aims to directly simulate the evolution of dust grains in ISM or galaxy evolution simulations. These simulations build off of the significant literature modelling single-sized dust in galaxies (e.g. McKinnon, Torrey & Vogelsberger 2016; Zhukovska et al. 2016; McKinnon et al. 2017; Popping, Somerville & Galametz 2017; Davé et al. 2019; Li, Narayanan & Davé 2019; Vijayan et al. 2019; Vogelsberger et al. 2019) and generally include models for the formation of dust in the ejecta of evolved stars, a range of growth processes, and the destruction of dust. Asano et al. (2013a) and Nozawa et al. (2015) developed simplified galaxy one-zone models in which they aggregated the equations that govern dust formation, growth by accretion and coagulation, and destruction by thermal sputtering and shattering in order to develop early numerical models for galaxy grain size distributions. These, coupled with an assumption for the optical properties of the grains (e.g. Draine & Lee 1984) result in an extinction curve. Hirashita (2015) developed a two-size grain model (small and large grains) which has since been applied (or similar variants of this model) to bona fide galaxy evolution simulations by a number of groups (Aoyama et al. 2018; Gjergo et al. 2018; Hou et al. 2019; Granato et al. 2021). To date, the only cosmological simulations to include dust with multiple sizes have employed this two-size approximation. At the same time, a number of studies have implemented dust with multiple (>2) grain sizes in idealized, non-cosmological galaxy simulations (McKinnon et al. 2018; Aoyama, Hirashita & Nagamine 2020). While these simulations represent a substantial step forward in their ability to self-consistently evolve the grain size distribution along with the fluid quantities in hydrodynamic galaxy simulations, they are unable to model the cosmological evolution of galaxies, and the attendant physical processes that may impact the dust masses and grain sizes.

In this paper, we develop the first cosmological hydrodynamic galaxy formation model to self-consistently model the evolution of dust grain sizes and masses in the ISM of galaxies over cosmic time. Here, we employ these simulations to understand, in specific, the origin of the inferred dust grain size distribution and observed extinction curve in Milky Way-mass galaxies at $z \sim 0$. We focus on the Milky Way in particular given the vast wealth of data for comparison to our model. Our goal is to develop a physical model that understands the observed range in extinction law slopes and bump strengths within the Milky Way and similar galaxies. This paper is organized as follows. In Section 2, we summarize the set up of the cosmological simulation, with a particular focus on the model for grain size evolution. In Section 3, we show our major results, and discuss both the origin of the Milky Way extinction law, as well as how and why the bump strengths and slopes vary. We provide discussion in Section 4, where we compare to other models, as well as discuss our uncertainties. In Section 5, we provide summary.

2 METHODS

2.1 Cosmological galaxy formation simulations

In this paper, we have run a series of cosmological simulations with the SIMBA galaxy formation physics suite, though with some significant updates to the dust model that we outline in Section 2.2. We refer the reader to Davé et al. (2019) for full details, and we summarize the salient points here. For reviews of broader numerical galaxy formation techniques, see Somerville & Davé (2015) and Vogelsberger et al. (2020).

The primary simulation we use here has 256^3 dark matter particles and 256^3 gas elements in a cube of $12h^{-1}$Mpc side length, and is run from $z = 99$ down to $z = 0$. Because of the small box size, we run eight such simulations, varying the random seeds for the initial conditions in order to produce different final galaxy populations. This enables us to build larger samples of galaxies while maintaining reasonable mass resolution. We assume a Planck16 (Planck Collaboration XIII 2016) concordant cosmology of $\Omega_m = 0.3$, $\Omega_\Lambda = 0.7$, $\Omega_b = 0.048$, $H_0 = 68$ km s^{-1} Mpc^{-1}, $\sigma_8 = 0.82$, and $n_s = 0.97$. Our run has a minimum gravitational softening length $\epsilon_{\rm min} = 0.25\,h^{-1}$ kpc, mass resolution $1.2 \times 10^7\,{\rm M}_\odot$ for dark matter particles and $2.28 \times 10^6\,{\rm M}_\odot$ for gas elements. The system is evolved using a forked version of the GIZMO cosmological gravity plus hydrodynamics solver (Hopkins 2015), in its Meshless Finite Mass (MFM) version. This code, modified from GADGET-3 (Springel 2005), evolves dark matter and gas elements together including gravity and pressure forces, handling shocks via a Riemann solver with no artificial viscosity.

Radiative cooling and photoionization heating are modelled using the GRACKLE-3.1 library (Smith et al. 2017), including metal cooling and non-equilibrium evolution of primordial elements. Star forma-

tion occurs in H_2 molecular gas, where the H_2 fraction is computed based on the sub-grid model of Krumholz, McKee & Tumlinson (2009) based on the metallicity and local column density, with minor modifications as described in Davé, Thompson & Hopkins (2016) to account for variations in numerical resolution. The star formation rate is given by the H_2 density divided by the dynamical time: SFR=$\epsilon_* \rho_{H2}/t_{dyn}$, where we use $\epsilon_* = 0.02$ (Kennicutt 1998). These stars drive winds in the interstellar medium. This form of feedback is modelled as a two-phase decoupled wind, with 30 per cent of wind particles ejected hot, i.e. with a temperature set by the supernova energy minus the wind kinetic energy. The modelled winds have an ejection probability that scales with the galaxy circular velocity and stellar mass (calculated on the fly via fast friends-of-friends galaxy identification). The nature of these scaling relations follow the results from higher resolution studies in the Feedback In Realistic Environments zoom simulation campaign (e.g. Hopkins et al. 2014, 2018; Muratov et al. 2015; Anglés-Alcázar et al. 2017b).

The chemical enrichment model tracks eleven elements (H, He, C, N, O, Ne, Mg, Si, S, Ca, Fe) during the simulation, with enrichment tracked from Type II supernovae (SNe II), Type Ia SNe (SNe Ia), and Asymptotic Giant Branch (AGB) stars. The yield tables employed are: Nomoto et al. (2006) for SN II yields, Iwamoto et al. (1999) for SN Ia yields, and AGB star enrichment following Oppenheimer & Davé (2006). Type Ia SNe and AGB wind heating are also included, along with ISM pressurization at a minimum level as required to resolve the Jeans mass in star-forming gas as described in Davé et al. (2016).

SIMBA incorporates black hole physics. Black holes are seeded and grown during the simulation via two-mode accretion. The first mode closely follows the torque-limited accretion model presented in Anglés-Alcázar et al. (2017a), and the second mode uses Bondi accretion, but solely from the hot gas component. The accretion energy is used to drive feedback that serves to quench galaxies, including a kinetic subgrid model for black hole feedback, along with X-ray energy feedback. SIMBA additionally includes a dust physics module to track the life-cycle of cosmic dust; we next describe this model, as well as improvements that we make to enable this study.

2.2 Dust model

In the original SIMBA model, we model dust approximated as a single grain size that passively advects with the gas (Li et al. 2019). In this paper, we have significantly updated this model to instead treat dust as its own particle that experiences grain–gas drag and gravity. Each particle contains a collection of spherical grains with a uniform mass density $\rho_{gr} = 2.4$ g cm^{-3} (Draine 2003) and radii a, and has a distribution of grain sizes that evolves owing to a range of physical processes.

To represent the grain size distribution, we divide $[\log a_{min}, \log a_{min}]$ into $N_{bin} = 41$ equally sized bins in log-space, where $a_{min} = 10^{-4}$ μm and $a_{max} = 1$ μm, and use N_k, the number of dust grains in the kth bin, to represent the discrete grain size distribution. Throughout the work, we apply piece-wise constant discretizations to the distribution. The new model allows us to track the evolution of dust mass and grain sizes at the same time. Our model is based on McKinnon et al. (2018) and we refer the interested reader to that paper for further details.

2.3 Dust production

A fraction of metals (C, O, Mg, Si, S, Ca, Fe) returned to the ISM by the ejecta of AGB stars and SNe II may condense into dust. We neglect the condensation of SNe Ia as it is a negligible source (see e.g. Nozawa, Kozasa & Habe 2006; Dwek 2016; Gioannini et al. 2017). To model the condensation, we follow the prescription of Li et al. (2019), which adopts the method of Dwek (1998) with updated condensation efficiencies. In the following, $m^j_{i,d}$ refers to the dust mass of the ith element (C, O, Mg, Si, S, Ca, Fe) produced by the jth stellar process (SN II or AGB stars), whereas $m^j_{i,ej}$ refers to the mass of ejecta from the jth process.

The mass of dust produced by AGB stars with a carbon-to-oxygen mass ratio C/O > 1 is expressed as

$$m^{AGB}_{i,d} = \begin{cases} \delta^{AGB}_C (m^{AGB}_{C,ej} - 0.75 m^{AGB}_{O,ej}), & i = C \\ 0, & \text{otherwise,} \end{cases} \quad (1)$$

where δ^{AGB}_i is the condensation efficiency of element i for AGB stars. The mass of dust produced by AGB stars with C/O < 1 is expressed as

$$m^{AGB}_{i,d} = \begin{cases} 0, & i = C \\ 16 \sum\limits_{k=Mg,Si,S,Ca,Fe} \delta^{AGB}_k m^{AGB}_{k,ej}/\mu_k, & i = O \\ \delta^{AGB}_i m^{AGB}_{i,ej}, & \text{otherwise,} \end{cases} \quad (2)$$

where μ_k is the mass of element k in atomic mass units. The mass of dust produced by SNe II is described as

$$m^{SNII}_{i,d} = \begin{cases} \delta^{SNII}_C m^{SNII}_{C,ej}, & i = C \\ 16 \sum\limits_{k=Mg,Si,S,Ca,Fe} \delta^{SNII}_k m^{SNII}_{k,ej}/\mu_k, & i = O \\ \delta^{SNII}_i m^{SNII}_{i,ej}, & \text{otherwise,} \end{cases} \quad (3)$$

where δ^{SNII}_i is the condensation efficiency of element i for SNe II. We choose fixed dust condensation efficiencies $\delta^{AGB}_i = 0.2$ and $\delta^{SNII}_i = 0.15$, guided by the model of the computation of Ferrarotti & Gail (2006) and Bianchi & Schneider (2007). We assume that the total carbon mass in the dust particles corresponds to the graphite mass, and the remainder goes to silicates, which gives the mass ratio of graphite-to-silicate grains.

Dust particles are stochastically created assuming that the creation is a Poisson process, following McKinnon et al. (2018). During a time-step, the probability of a star or gas particle of mass M spawning a dust particle with mass $M_d = \beta M$ ($\beta = 0.02$ in our simulation) is

$$p_d = \frac{M}{M_d}\left[1 - \exp\left(-\frac{m_{i,d}}{M}\right)\right]. \quad (4)$$

A random number is drawn between 0 and 1. If the number is smaller than p_d then a dust particle is created.

Once the decision has been made to create a dust particle, the initial grain size distribution is assigned according to the type of the stellar process. We assume the initial grain size distribution is

$$\frac{\partial n}{\partial \log a} = \frac{C}{a^p} \exp\left(\frac{\ln^2(a/a_0)}{2\sigma^2}\right), \quad (5)$$

where C is a normalization constant, $a_0 = 0.1$μm. $(p, \sigma) = (4, 0.47)$ for dust produced by AGB stars and $(p, \sigma) = (0, 0.6)$ for SN II, following the work by Asano et al. (2013b).

We then draw a total number of $N = 10^4$ particles with grain radii a between $\log a_{min}$ and $\log a_{max}$ using the Metropolis–Hasting algorithm to sample the initial grain size distribution, with N_k particles in the kth bin described in Section 2.2. N_k is later evolved based on the processes described in the following sections. Note that we assume that the silicate grains and graphite grains have the same size distributions in this work, and the distributions are not evolved separately for different species.

2.4 Dust growth

Once dust particles are produced, they are able to grow by accreting neighbouring gas-phase metals. Following Dwek (1998), the growth rate of grain radius a can be expressed as:

$$\left(\frac{\mathrm{d}a}{\mathrm{d}t}\right)_{\mathrm{grow}} = \frac{a}{\tau_{\mathrm{accr}}}, \tag{6}$$

where τ_{accr} is the characteristic accretion time-scale. Following Hirashita (2000), which assumes the process is a two-body collision, the time-scale τ_{accr} is

$$\tau_{\mathrm{accr}} = \tau_{\mathrm{ref}} \left(\frac{a}{a_{\mathrm{ref}}}\right) \left(\frac{\rho_{\mathrm{ref}}}{\rho_{\mathrm{g}}}\right) \left(\frac{T_{\mathrm{ref}}}{T_{\mathrm{g}}}\right)^{\frac{1}{2}} \left(\frac{Z_{\mathrm{ref}}}{Z_{\mathrm{g}}}\right), \tag{7}$$

where $a_{\mathrm{ref}} = 0.1\,\mu\mathrm{m}$ and ρ_{g}, T_{g}, and Z_{g} are the neighbouring gas density, temperature, and metallicity, respectively. τ_{ref}, ρ_{ref}, T_{ref}, and Z_{ref} are the reference values correspondingly, which have $(\tau_{\mathrm{ref}}/\mathrm{Gyr}, \rho_{\mathrm{ref}}/m_{\mathrm{H}}\,\mathrm{cm}^{-3}, T_{\mathrm{ref}}/\mathrm{K}, Z_{\mathrm{ref}}) = (0.03, 100, 20, Z_{\odot})$. We take $Z_{\odot} = 0.0134$ throughout this paper based on Asplund et al. (2009).

To compute the grain growth time-scale in equation (7), ρ_{g}, T_{g}, and Z_{g} are evaluated by smoothing properties of $N_{\mathrm{ngb}} \sim 32$ neighbouring gas particles in a kernel-weighted way. To this end, we first iteratively solve the smoothing length h_{dg} via

$$N_{\mathrm{ngb}} = \frac{4\pi h_{\mathrm{dg}}^3}{3} \sum_{r_i < h_{\mathrm{dg}}} W\left(r_i, h_{\mathrm{dg}}\right), \tag{8}$$

where r_i is the distance from the dust particle to the ith gas particle within a sphere with a radius h_{dg} and $W(r, h)$ is the cubic spline kernel.

Then we can compute gas properties via

$$\rho_{\mathrm{g}} = \sum_{i=1}^{N_{\mathrm{ngb}}} M_i W\left(r_i, h_{\mathrm{dg}}\right) \tag{9}$$

and

$$T_{\mathrm{g}} = \frac{\sum_{i=1}^{N_{\mathrm{ngb}}} M_i T_i W\left(r_i, h_{\mathrm{dg}}\right)}{\rho_{\mathrm{g}}}, \tag{10}$$

where M_i and T_i represent the mass and temperature of ith neighbouring gas cell, respectively. Other gas properties needed for dust physics are evaluated in the same manner as equation (10).

2.5 Dust destruction

2.5.1 *Thermal sputtering*

Dust grains can be eroded by colliding with thermally exited gas especially in hot haloes, a process known as 'sputtering' (Barlow 1978; Draine & Salpeter 1979; Tielens et al. 1994). In this work, we adopt an analytic approximation derived by Tsai & Mathews (1995):

$$\left(\frac{\mathrm{d}a}{\mathrm{d}t}\right)_{\mathrm{sp}} = -\frac{a}{\tau_{\mathrm{sp}}}, \tag{11}$$

where the characteristic time-scale

$$\tau_{\mathrm{sp}} \sim (0.17\ \mathrm{Gyr}) \left(\frac{a}{a_{\mathrm{ref}}}\right) \left(\frac{10^{-27}\ \mathrm{g\ cm}^{-3}}{\rho_g}\right) \left[\left(\frac{T_0}{T}\right)^{\omega} + 1\right], \tag{12}$$

where $\omega = 2.5$ controls the low-temperature scaling of the sputtering rate and $T_0 = 2 \times 10^6$ K is the temperature above which the sputtering rate flattens.

2.5.2 *Dust destruction via SN shocks*

In addition to thermal sputtering, SN blast waves offer another approach to destroying dust grains by enhancing inertia and thermal sputtering (Dwek & Scalo 1980; Seab & Shull 1983; McKee et al. 1987; McKee 1989). The SN shocks shifts the grain size distribution to smaller sizes. We follow McKinnon et al. (2018), who build off of Yamasawa et al. (2011) and Asano et al. (2013a) to determine the evolution of grain size distribution caused by SN shocks. This method is parametrized by a conversion efficiency $\xi(a, a')$ such that $\xi(a, a')\mathrm{d}a$ denotes the fraction of grains starting with sizes $[a', a' + \mathrm{d}a]$ that end up with sizes $[a, a + \mathrm{d}a]$. The $\xi(a, a')$ values are calculated using a detailed model of dust destruction in SN blast waves developed by Nozawa et al. (2006). The rate of change of number of grains in the kth bin is

$$\left(\frac{\mathrm{d}N_k}{\mathrm{d}t}\right)_{\mathrm{de}} = \frac{\gamma M_s}{M_g} \left(\sum_{i=1}^{N_{\mathrm{bin}}} N_i(t)\xi(a_k, a_i)(a_{k+1} - a_k) - N_k(t)\right), \tag{13}$$

where M_g is the neighbouring gas mass, γ is the neighbouring SN II rate, and M_s is the mass of neighbouring gas shocked to at least $100\,\mathrm{km\,s}^{-1}$ per SN event. Because our simulations do not resolve the multiphase ISM, we apply the Sedov–Taylor solution to a homogeneous medium of $n_{\mathrm{H}} = 0.13\,\mathrm{cm}^{-3}$ (the minimum SF threshold density of our simulations) following McKee (1989), yielding:

$$M_s = 6800 E_{\mathrm{SNII},51} \left(\frac{v_s}{100\ \mathrm{km\ s}^{-1}}\right)^{-2} M_{\odot}, \tag{14}$$

where $E_{\mathrm{SN\,II},\,51}$ is the energy released by a SN II in units of 10^{51} erg, and $v_s \sim 100\,\mathrm{km\,s}^{-1}$ is the shock wave speed. The resulting change rate of mass of grains in bin k (M_k) is

$$\left(\frac{\mathrm{d}M_k}{\mathrm{d}t}\right)_{\mathrm{de}} = \frac{\gamma M_s}{M_g} \left\{\sum_{i=1}^{N_{\mathrm{bin}}} \left[N_i(t)\xi(a_k, a_i)\left(\frac{\pi\rho_{\mathrm{gr}}a^4}{3}\right)\right]_{a_k}^{a_{k+1}} - M_k(t)\right\} \tag{15}$$

2.6 Grain shattering and coagulation

Grain–grain collisional processes including shattering and coagulation, though conserve the dust mass, could significantly shape the grain size distributions. In this work, we follow the approach of McKinnon et al. (2018). For shattering, the mass evolution for grain size bin k is

$$\frac{\mathrm{d}M_k}{\mathrm{d}t} = -\frac{\pi\rho_{\mathrm{d}}}{M_{\mathrm{d}}} \left(\sum_{k=0}^{N-1} v_{\mathrm{rel}}(a_i, a_k)\mathbb{1}_{v_{\mathrm{rel}} > v_{\mathrm{th}}}(a_i, a_k) m_i I^{i,k} - \frac{1}{2}\sum_{k=0}^{N-1}\sum_{j=0}^{N-1} v_{\mathrm{rel}}(a_k, a_j)\mathbb{1}_{v_{\mathrm{rel}} > v_{\mathrm{th}}}(a_k, a_j) m_{\mathrm{col}}^{k,j}(i) I^{k,j}\right), \tag{16}$$

where ρ_{d} is the mass density of dust, $v_{\mathrm{rel}}(a_i, a_k)$ is the relative velocity of two grains at grain size bins i and k, respectively (we assume grains within one dust particle and one size bin have the same velocity for simplicity), $v_{\mathrm{th}}(a_i, a_k)$ is the threshold velocity where shattering or coagulation can happen, $\mathbb{1}_{v_{\mathrm{rel}} > v_{\mathrm{th}}}(a_i, a_k)$ is the indicator function in the form

$$\mathbb{1}_{v_{\mathrm{rel}} > v_{\mathrm{th}}}(a_i, a_k) = \begin{cases} 1, & v_{\mathrm{rel}}(a_i, a_k) > v_{\mathrm{th}}(a_i, a_k) \\ 0, & \text{otherwise,} \end{cases} \tag{17}$$

m_i is the average mass of a grain in bin i, $m_{\rm col}^{k,j}(i)$ is the resulting mass entering bin i due to the collision between grains in bins k and j, and

$$I^{k,j} = \int_{a_k}^{a_{k+1}} \int_{a_j}^{a_{j+1}} \frac{N_k N_j}{(a_{k+1}-a_k)(a_{j+1}-a_j)}(a_1+a_2)^2 {\rm d}a_2 {\rm d}a_1. \quad (18)$$

For coagulation, the mass evolution is generally the same as equation (16) but $\mathbb{1}_{v_{\rm rel}>v_{\rm th}}$ is replaced by $\mathbb{1}_{v_{\rm rel}<v_{\rm th}}$.

To calculate the relative velocity $v_{\rm rel}$, we basically follow the calculation by equation (C1)–(C4) of Hirashita & Aoyama (2019) where grain velocity is set by the drag force of the turbulent gas flow, but assume the turbulent velocity has a supersonic power spectrum instead of the Kolmogorov power spectrum

$$v = v_J \left(\frac{l}{L_J}\right)^{\frac{1}{2}}, \quad (19)$$

giving the velocity dispersion of grains with radii a:

$$\sigma_{\rm gr} = 0.06 \left(\frac{v_J}{c_{\rm g}}\right)^2 \left(\frac{a}{0.1\,\mu{\rm m}}\right) \left(\frac{\rho_{\rm g}}{1\,{\rm cm}^{-3}\times m_{\rm H}}\right)^{-\frac{1}{2}} \left(\frac{\rho_{\rm gr}}{2.4{\rm g\ cm}^{-3}}\right) {\rm km\,s}^{-1}, \quad (20)$$

where $c_{\rm g}$ is the local speed of sound and $v_J = 0.7(L_J/1{\rm pc})^{1/2}$ km s^{-1} (Solomon et al. 1987) is the turbulent velocity at the size of eddies with the Jeans Length $L_J \equiv (\pi c_{\rm g}^2/G\rho_{\rm g})^{1/2}/2$. The relative velocities of grains are then calculated via x, y, z components of grain velocities randomly drawn from Gaussian distributions $N(0, \sigma_{\rm gr}^2/3)$.

For shattering, Jones, Tielens & Hollenbach (1996) uses a threshold velocity $v_{\rm th} = 2.7$ km s^{-1} for silicate grains and $v_{\rm th} = 1.2$ km s^{-1} for graphite grains. We adopt $v_{\rm th} = 2$ km s^{-1} for all grain species, for we do not track detailed evolution of multiple grain species. The computation of $m_{\rm col}^{k,j}(i)$ follows Section 2.3 of Hirashita & Yan (2009), which considers partial or complete fragmentation of colliding grains.

For coagulation, the threshold velocity $v_{\rm th}$ is computed via equation (8) of Hirashita & Yan (2009), dependent on grain sizes a_k and a_j of two colliding grains, and

$$m_{\rm col}^{k,j}(i) = \begin{cases} m_k + m_j, & \log a_i + \frac{1}{2}\Delta(i) \le \frac{m_k+m_j}{4\pi\rho_{\rm gr}/3} < \log a_{i+1} - \frac{1}{2}\Delta(i), \\ 0, & \text{otherwise}, \end{cases} \quad (21)$$

where $\Delta(i) \equiv \log a_{i+1} - \log a_i$.

Note, SIMBA adopted the Krumholz et al. (2009) model to compute the phase transition of ISM (e.g. the mass fraction of molecular H2, star formation, and temperature). During computation this model boosts the density of gas (from the simulation) by a factor of C (C scales with the resolution, see Davé et al. 2019) to account for the subgrid clumping of the gas in the ISM, which gives proper ISM phases for underresolved regions. On the other hand, the choice of free parameters (tuned to match the dust mass function as is in Li et al. 2019) in the computation of growth rate innately boosts the density to account for the subgrid clumping of the gas in the ISM. With these treatments the model is able to account for subgrid clumping of gas/dust densities and give a proper time-scale for grain growth in underresolved dense regions where rapid grain growth happens.

2.6.1 Dust consumption via star formation

The mass of dust particles is reduced when star particles are created in the neighborhood, a process known as 'astration'. To evaluate the amount of dust mass consumed by star particles, we first compute the weight for the ith neighbouring gas or star particle within the sphere with a radius $h_{\rm dg}$:

$$w_i = m_i W(r_i, h_{\rm dg}), \quad (22)$$

where $h_{\rm dg}$ is determined by equation (8). Then a fraction f_j of mass of the dust particle is consumed by the jth nascent star particle, where

$$f_j = \frac{w_j}{\sum_{r_i<h_{\rm dg}} w_i}. \quad (23)$$

The metal mass and momentum are assumed to be conserved during this process.

2.7 Dust dynamics

The motion of dust particles follow the pressure-less fluid dynamics, interacting with the gas fluid via gravity and a drag force given by:

$$\frac{{\rm d}v_g}{{\rm d}t} = a_{\rm drag} + a_{\rm ex}, \quad (24)$$

where $a_{\rm ex}$ denotes external sources of acceleration (in particular gravity for our simulations), and v_g is the gas velocity. The acceleration caused by the drag force $a_{\rm drag}$ is given by

$$a_{\rm drag} = -\frac{v_{\rm d} - v_{\rm g}}{t_s}, \quad (25)$$

where v_d is the dust velocity, and the stopping time t_s is given by

$$t_s = \frac{M_{\rm d}\rho_{\rm g}}{K_s(\rho_{\rm g}+\rho_{\rm d})} \sim \frac{M_{\rm d}}{K_s} \quad (26)$$

as the dust density $\rho_{\rm d}$ typically satisfies $\rho_{\rm d}/\rho_{\rm g} \ll 1$ in the cosmological simulations. Here K_s is the drag coefficient (described below).

In the cosmological simulations, the typical radii of dust grains $a \ll 9\lambda/4$ where λ is the mean free path of gas particles, corresponding to the Epstein regime (Epstein 1924). The drag coefficient in this regime is given by

$$K_s = \frac{8\sqrt{2\pi}c_{\rm g}a^2\rho_{\rm g}}{3\sqrt{\gamma}}, \quad (27)$$

where a is the grain radius, and γ is the adiabatic index. This gives

$$t_s \sim \frac{M_{\rm d}}{K_s} = \frac{\sqrt{\pi\gamma}a\rho_{\rm gr}}{2\sqrt{2}\rho_{\rm g}c_s}. \quad (28)$$

This assumes subsonic dust-to-gas relative velocities and should be corrected by the following fit (Draine & Salpeter 1979):

$$t_s = \frac{\sqrt{\pi\gamma}a\rho_{\rm grain}}{2\sqrt{2}\rho_{\rm g}c_s}\left(1+\frac{9\pi}{128}\left|\frac{v_{\rm d}-v_{\rm g}}{c_s}\right|^2\right)^{-\frac{1}{2}} \quad (29)$$

in order to be applied to supersonic dust-to-gas relative velocity.

The time integration follows the semi-implicit time-stepping approaches detailed in Hopkins & Lee (2016) to lift the strict time-stepping requirement ${\rm d}t < t_s$ for an explicit integrator when the stopping time t_s is much smaller than the time-scale of other accelerations, which is typical of the cosmological simulations where dust couples with gas in most regions. The integrator can be expressed by

$$v_{\rm d}(t+{\rm d}t) = \tilde{v}_{\rm d}(t+{\rm d}t) - \xi[\tilde{v}_{\rm d}(t+{\rm d}t) - \tilde{v}_{\rm g}(t+{\rm d}t)] + [\xi({\rm d}t+t_s) - {\rm d}t] + \frac{\nabla P}{\rho_{\rm g}}, \quad (30)$$

where $\tilde{v}$ denotes the velocity at time $t+{\rm d}t$ after non-drag kicks are applied but before the drag force is applied, and $\xi = 1-\exp(-{\rm d}t/t_s)$. This gives a Courant–Friedrichs–Lewy (CFL) type time-step

$${\rm d}t_{\rm CFL} = \frac{C_{\rm CFL}h_{\rm d}}{\sqrt{c_s^2+|v_{\rm d}-v_{\rm g}|^2}}, \quad (31)$$

where $h_{\rm d}$ is the smoothing length for dust particles.

Table 1. Simulation free parameters.

Parameter	Description	Value
Thermal sputtering		
$\rho_{\rm gr}$	Density of solid matters within grains (g cm^{-3})[a]	2.4
Production	–	–
$\delta_{i,\rm dust}^{\rm AGB,C/O>1}$	Condensation efficiency[b]	0.2 for i = C
	–	0 otherwise
$\delta_{i,\rm dust}^{\rm AGB,C/O<1}$	–	0 for i = O
	–	0.2 otherwise
$\delta_{i,\rm dust}^{\rm SNII}$	–	0.15 for i = C
	–	0.15 otherwise
Growth	–	–
$\rho^{\rm ref}$	Reference density (g cm^{-3})	2.3×10^{-22}
$T^{\rm ref}$	Reference temperature (K)	20
$\tau_{\rm g}^{\rm ref}$	Growth time-scale with $T = T^{\rm ref}$ and $\rho = \rho^{\rm ref}$ (Myr)[c]	10
Destruction (SN shocks)	–	–
$E_{\rm SN,\,51}$	Energy per SN (10^{51} erg)[d]	1.0

Notes. [a] Jones et al. (1996), Draine (2003).
[b] Dwek (1998), McKinnon et al. (2017), Popping et al. (2017)
[c] Dwek (1998), Zhukovska (2014), McKinnon et al. (2017), Popping et al. (2017)
[d] McKee (1989).

In order to track the formation and evolution of dust grains and their sizes, we implement dust production via condensation of stellar ejecta, dust growth via accretion of gas-phase metals, dust destruction via shock waves and thermal sputtering, and grain coagulation and shattering. The choice of free parameters is shown in Table 1, with further discussion in Li et al. (2019).

2.8 Galaxy identification and tracking

Haloes are identified using a 3D friends-of-friends algorithm within GIZMO, with a linking length of 0.2 times the mean interparticle spacing. Galaxies are identified via a 6D friends-of-friends technique within the publicly available galaxy analysis tool CAESAR.[2] The minimum number of baryonic particles for an identified galaxy is 24, leading to a minimum baryonic mass $\sim$5.47 $\times$ 10^7 M$_\odot$. We consider galaxies at $z = 0$ within 0.3 dex of a stellar mass of 6×10^{10} M$_\odot$ (Licquia & Newman 2015) and a halo mass of 1.6×10^{12} M$_\odot$ (Boylan-Kolchin et al. 2013) as reasonable analogues to the Milky Way. Note, this choice is out of the consideration of statistical significance without trying to match the morphology. In total, we identify 12 galaxies at $z = 0$ within this mass range. These galaxies have metallicities in the range [0.33$Z_\odot$, 2.19$Z_\odot$] and gas mass [5.52×10^9 M$_\odot$, 2.84×10^{10} M$_\odot$]. Furthermore, we trace back their most massive progenitors at each earlier snapshot to track the evolutionary history of these galaxies.

2.9 Validation: Global dust-to-gas ratios

Before proceeding, we present a validation of this model as applied to our simulations. The scaling relation between dust-to-gas ratio (DGR) and gas-phase metallicity represents an important constraint on models of the dust life-cycle. In Fig. 1, we plot the modelled $z = 0$ DGR against the galaxy gas-phase metallicity Z for all simulated galaxies, colour-coded by specific star formation rates (sSFR = SFR/M_*). The coloured points (viridis map) show the simulated galaxies at $z = 0$, while the black diamonds and grey crosses show the observational constraints from Rémy-Ruyer et al. (2014) (assuming a metallicity-dependent CO-to-H$_2$ conversion factor) and De Vis et al. (2019). We see excellent correspondence between our model DGR and the observational constraints at both high and low metallicity.

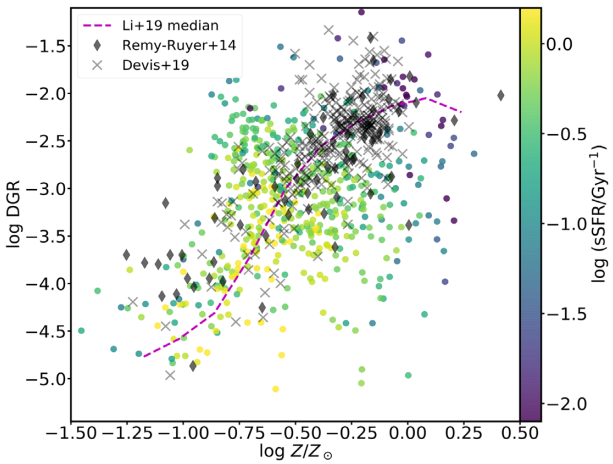

Figure 1. Verification of our methodology and model results by comparing the simulated dust-to-gas ratio versus metallicity relation to observed galaxies at $z = 0$. The yellow→purple data (viridis colour map) show all of our simulated galaxies at $z = 0$ (i.e. not just Milky Way-mass), while the black diamonds and crosses show the observational constraints by Rémy-Ruyer et al. (2014) (assuming a metallicity-dependent CO-to-H$_2$ conversion factor) and De Vis et al. (2019), respectively. The colours of the simulated data quantify their specific star formation rate. The dashed magenta line denotes the running median of the dust-to-gas ratio versus gas-phase metallicity relation from our previous passive dust model (Li et al. 2019). Our model reproduces the general observed trend of increasing dust-to-gas ratio and metallicity.

We see roughly a linear increase of DGR as a function of Z at $Z \lesssim 0.15Z_\odot$ and $Z \gtrsim 0.5Z_\odot$ which correspond to the regimes dominated by dust production and dust growth, respectively. There is a non-linear rise from $Z \sim 0.15Z_\odot$ to $Z \sim 0.5Z_\odot$ which corresponds to the transition from production-dominated regime to growth-dominated regime. We also compare this scaling relation to the relation we get from the passive dust model of Li et al. (2019), the running median of

[2] https://github.com/dnarayanan/caesar

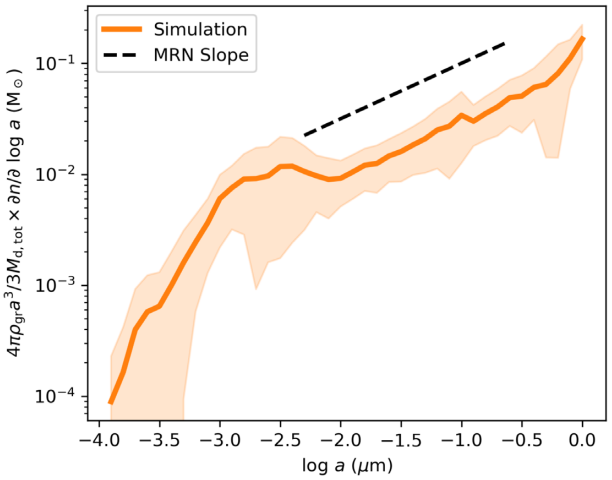

Figure 2. Mass-weighted grain size distributions for Milky Way analogues in our simulation (the peach-coloured line shows the mean, while the shaded region shows the 1σ dispersion amongst our sample of galaxies). Our model Milky Way analogues at $z = 0$ produce a diverse range of grain size distributions, though with slopes comparable to a traditional MRN distribution (dashed line – note, the MRN distribution normalization is arbitrary, and we manually offset it from our model galaxies to enhance clarity). This said, the diversity in the small grain size distributions drives variation in the UV/optical slopes of the extinction curves, while the bump strengths are more closely tied to the fraction of graphites versus silicates in a galaxy.

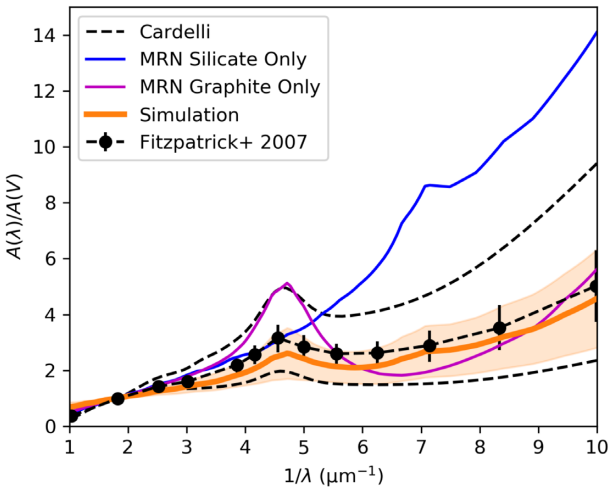

Figure 3. Model Milky Way mass galaxies formed at $z = 0$ in our model (the mean value and the standard deviation denoted by a solid peach-coloured line and a shaded region) exhibit dust extinction laws comparable to the range observed in the Milky Way. The dashed lines denote the bounds of the Cardelli et al. (1989) inferred curves (for a R_V range of [2,5]), while the dash-dot line denotes the average Fitzpatrick & Massa (2007) constraint. The extinction curves assuming an MRN grain size distribution and a grain composition with 100 per cent graphites or silicates are denoted by magenta and blue lines, respectively. These curves are produced by convolving the grain size distributions (c.f. Fig. 2) with assumed extinction efficiencies of the dust grains for graphites and silicates (Laor & Draine 1993). That the slopes and bump strengths match those of the Milky Way is a reflection of the dominance of grain growth over destruction processes in metal-rich environments. See the text for details.

which is denoted by dashed magenta lines. The relation from current model generally follows the trend we get from the passive dust model. We see that there is large scatter as dust growth becomes dominant. This indicates the impact of the variance in mass-averaged grain sizes for dust particles instead of a single grain size $a = 0.1\,\mu$m assumed by our previous work (c.f. equation 7). This figure also shows galaxies with active on-going star formation tend to have lower DGR while highly evolved galaxies close to quenching have higher DGR as abundant metals from AGBs and SNe are rapidly accreted into dust grains, which is consistent with our previous study.

3 RESULTS

3.1 Extinction curves in milky way mass galaxies

We first ask the question: do our model galaxies with a comparable stellar mass and halo mass as the Milky Way have extinction curves comparable to observed constraints? In Fig. 2, we plot the dust size distribution for all of our Milky Way analogues at $z = 0$, and compare this to a Mathis et al. (1977) ('MRN') power-law slope. While there is significant diversity in the grain size distributions (a topic we will return to later in this paper), the bulk of the distribution functions have slopes comparable to the MRN slope in the size ranges of interest. The primary differences in the curves are in the lowest size bins, which, as we will show, have to do with the dust growth history that most closely ties to the metal enrichment history in the galaxy. We note that our simulations have not been tuned to reproduce this result, but rather the size distributions are a natural consequence of two dominant competing processes i.e. grain growth and destruction processes in our model. We discuss this in more detail shortly.

In order to compute the extinction curve from the model grain size distributions, we require knowing the extinction efficiencies (i.e. the ratio of the extinction to geometric cross-sections) of our grains. Here, we assume the models of Laor & Draine (1993), who quantify these cross-section ratios for silicates and graphites. We therefore require assuming a silicate to graphite abundance ratio alongside our computed grain size distributions. Within our dust superparticles, we assume that the graphite mass corresponds to the total carbon mass, and the remainder is silicates. We further assume that the silicate grains and graphite grains have the same size distribution. We describe the computation of extinction curves in more detail in Appendix A. In Fig. 3, we show the extinction curve for grains with an MRN size distribution that are comprised of pure graphites (magenta line) and pure silicates (blue line) in order to help the reader interpret our model results. Note that we use the average grain-size distributions of all dust particles in each galaxy to derive extinction curves instead of particles along a certain line of sight.

In Fig. 3, we show the derived extinction curves from our Milky Way-mass galaxies. The yellow line and the shaded region shows the mean extinction curve and the standard deviation of the galaxies, while the dashed lines show the range of observationally derived extinction curves as parametrized by R_V in the Galaxy (Cardelli et al. 1989) and the sightline averaged result from Fitzpatrick & Massa (2007). We additionally show the extinction laws assuming an MRN grain size distribution and a grain composition with 100 per cent graphites or silicates. This demonstrates that a large graphite-to-silicate mass ratio contributes to strong 2175 Å bumps while a small ratio leads to a bump-less extinction curve. Generally, our model Milky Way-mass galaxies show diversity in their extinction curves, though demonstrate excellent correspondence with the observed range in the Milky Way. We see a range of slopes and bump strengths. In the remaining subsections, we unpack the origin of this diversity in the curves.

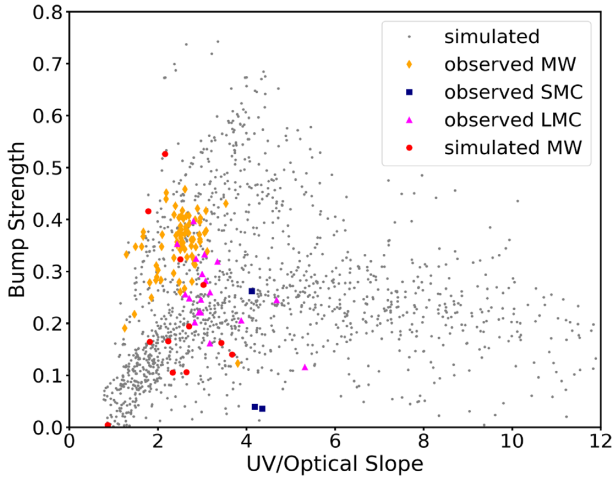

Figure 4. UV bump strength versus UV-optical slope relation. The grey points show all galaxies in our model, and orange, blue, and pink points show the observed Milky Way, SMC and LMC data points (Fitzpatrick & Massa 1990; Fitzpatrick 1999; Clayton, Gordon & Wolff 2000; Gordon et al. 2003; Fitzpatrick & Massa 2007, 2009; Nataf et al. 2016). We show all of our galaxies simply to build statistics. The slopes in our models vary monotonically with metallicity, while the bump strength depends on the graphite-to-silicate ratio (which shows substantial dispersion at $z = 0$). As a result, in our simulations there is little bump-slope relation in Milky Way analogues. At the same time, individual observed sightlines in the Galaxy may have a similar graphite-to-silicate ratio, and therefore, a loose trend between the bump and slope (Salim & Narayanan 2020). Our model cannot account for the small bump strengths of the observed LMC and SMC (see Section 4.2 for details).

3.2 What drives the diversity of extinction curves?

To characterize the extinction curves and facilitate the comparison amongst different curves quantitatively, we follow the review of Salim & Narayanan (2020) in defining two parameters: the overall UV-optical slope S and the 2175 Å absorption bump strength B.

As a high-level characterization of a curve, the overall UV-optical slope is defined as the ratio of extinction at 1500 Å and in the V-band:

$$\mathrm{S} \equiv A_{1500}/A_V, \tag{32}$$

which generally reflects the relative extinction in the UV band compared to the optical band. The bump strength is defined as the ratio of extra extinction due to the bump at 2175 Å to the base-line extinction at 2175 Å

$$B \equiv A_{\mathrm{bump}}/A_{2175,0}, \tag{33}$$

where the extinction due to the bump can be estimated by

$$A_{\mathrm{bump}} = A_{2175} - A_{2175,0}, \tag{34}$$

where the base-line extinction in the absence of the bump can be estimated by

$$A_{2175,0} \equiv (0.33A_{1500} + 0.67A_{3000}). \tag{35}$$

In Fig. 4, we show the bump strength versus optical slope relation and UV slope versus optical slope relation for all of our model galaxies (i.e. not just Milky Way-mass galaxies). We additionally show the observational constraints in both spaces for the Galaxy and Magellanic Clouds by Fitzpatrick (1999), Fitzpatrick & Massa (2007, 2009), Clayton et al. (2000), Nataf et al. (2016), and Gordon et al. (2003) as light grey points. Our model Milky Way analogues have a comparable scatter in bump-slope space as the observed Galactic sightlines, though a larger dynamic range (as we will show, this larger dynamic range owes to variations in the graphite-to-silicate ratio).

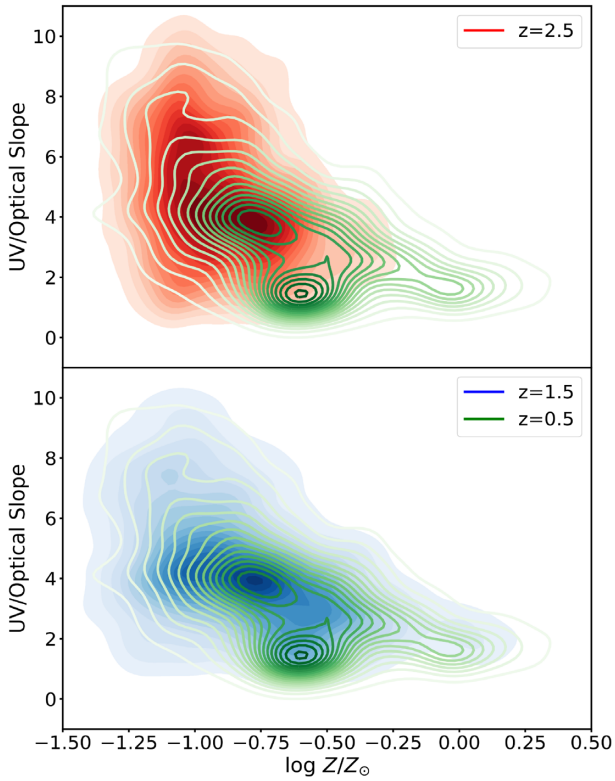

Figure 5. Contour plots of the UV-optical slopes S (c.f. equation 32) of extinction curves against metallicities of the galaxies from our cosmological simulation. The red, blue, and green contours represent galaxies at $z = 2.5$, $z = 1.5$, and $z = 0.5$, respectively. We show all galaxies to develop sufficient statistics (i.e. not just Milky Way analogues). As in Fig. 6, as the metallicity increases at all redshifts, we see decreased slopes at these redshifts owing to highly efficient grain growth.

Understanding the origin of the Milky Way extinction law slopes and the relationship between bump strengths and slopes originates in the metallicity and dust growth history of the galaxy. To illustrate this, we first rewrite equation (33) as $B \equiv (A_{\mathrm{bump}}/A_V)/(A_{2175,0}/A_V)$. $(A_{2175,0}/A_V)$ tends to increase as the slopes of the extinction curves become steeper. On the other hand, (A_{bump}/A_V) correlates with fraction of small graphite grains (we remind the reader of the extinction law shapes for pure graphites and pure silicates in Fig. 3). We then show the relation between the slopes of the extinction curves and the gas-phase metallicities for all model galaxies (for better statistics) at $z \leq 2.5$ in Fig. 5. There is an anticorrelation between the slopes and the metallicities, which is especially tight at $Z \gtrsim 0.3Z_\odot$. We see large scatter in the low metallicity regime ($Z \lesssim 0.3Z_\odot$). where dust production via AGB or SNe is the main sources of the dust mass. In the situation that there is not enough time for collisional processes to create a sufficient small grain population, the extinction curves tend to be relatively flat. However, given enough time for collisional processes, the number of small grains will build up and lead to a steep extinction curve. In the regime of $Z \gtrsim 0.3Z_\odot$, the highly efficient growth moves small grains (defined notionally here as $a \lesssim 0.06\,\mu$m) to the large grain regime ($a \gtrsim 0.06\,\mu$m), and consequently flattens the extinction curves. We hereafter define the 'Small-to-Large Ratio' (STL) as the mass fraction of grains smaller than 0.06 μm compared to those larger than this notional size. This

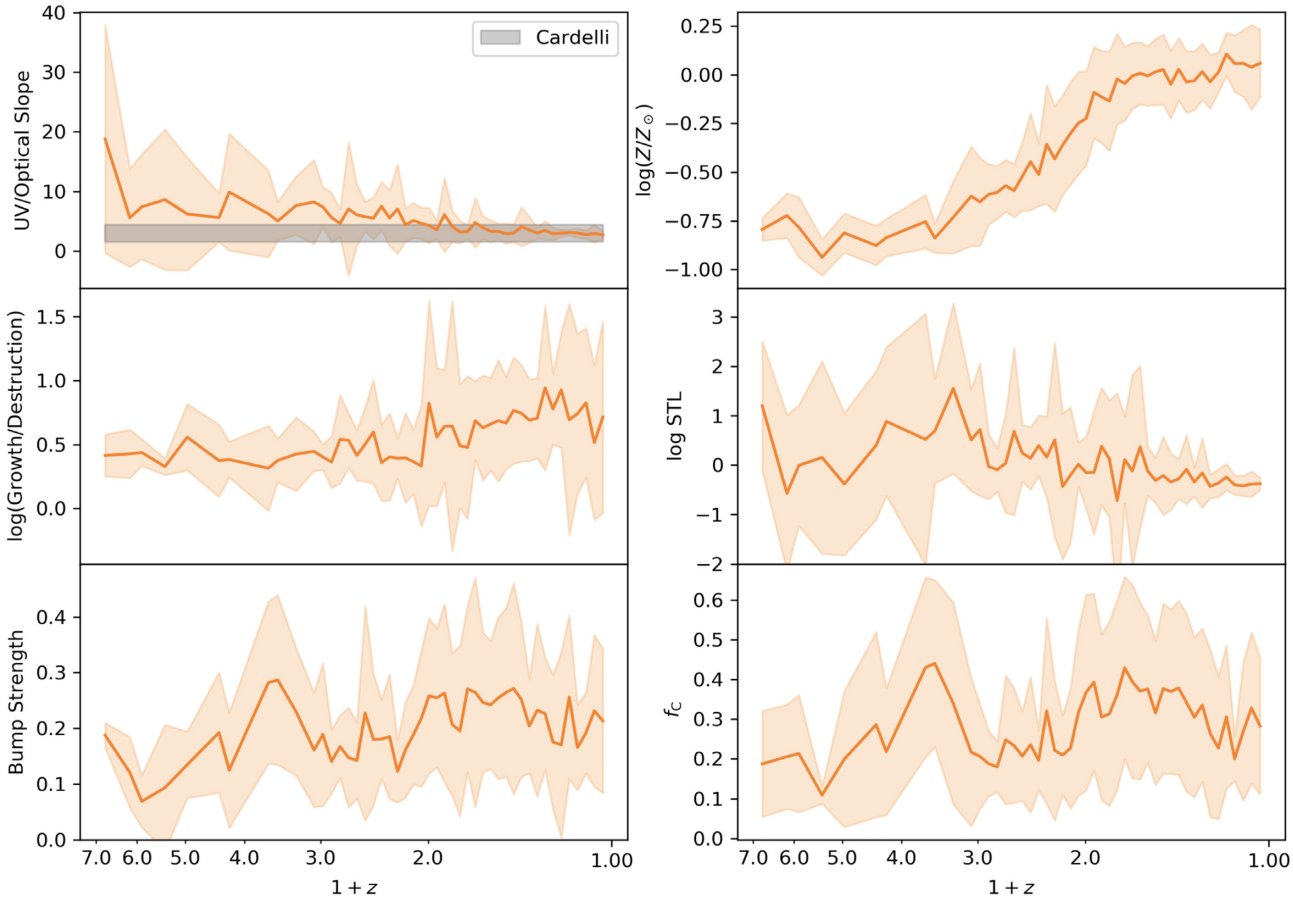

Figure 6. The slopes of extinction curves anticorrelate with metallicity in our model such that the slopes are reduced at late times/high metallicities. This owes primarily to increased grain growth rates in high metal density environments. The bump strengths correlate with the graphite to total dust mass ratio such that a larger value leads to a bigger bump. The subpanels here illustrate these trends, with details in Section 3.2. Clockwise from top left: Top left-hand panel**:** We show the evolution of the UV/optical slope for 1 Milky Way analogue in our simulations (with the yellow shaded region showing dispersion for all progenitors of the same mass at a given redshift). The observed Milky Way range (Cardelli et al. 1989) is shown by the light grey horizontal shaded region. Top right-hand panel: Evolution of the gas-phase metallicity. Middle right-hand panel: Evolution of the small grain to large grain ratio. Bottom right-hand panel: Evolution of graphite to total dust mass ratio. Bottom left-hand panel: Evolution of the bump strength. Middle left-hand panel: Evolution of the ratio of grain growth to dust destruction rate. The destruction includes thermal sputtering and destruction in SN shocks.

leads to decreasing bump strengths following flattening slopes as metallicities increase, provided the graphite to total dust mass ratios (f_C) do not vary (which is the case for observed extinction curves along different lines of sight in the Milky Way). In reality, however, f_C span a large range even though STL stays the same. This results in substantial large scatter in our modelled $A_{\rm bump}/A_V$ relation, as well as the resultant *B*–*S* relation, with the upper bound corresponding to higher graphite-to-silicate ratio.

In Fig. 6, we quantify the previous argument. Here, we plot the redshift evolution of the (clockwise from top left) redshift evolution of the UV/optical slope of one of our model MW galaxies, gas phase metallicity, STL, the graphite-to-silicate ratio (f_c), the bump strength, and the ratio of grain growth to destruction rate (including the thermal sputtering rate and the rate of destruction in SN shocks). To generate this plot, we follow the main progenitor of one of our MW analogues backwards in time via progenitors with the most number of stars in common (the solid orange lines). The galaxy we choose has the $z = 0$ stellar mass of $6.04 \times 10^{10}\,{\rm M}_\odot$, closest to the measured stellar mass of the Milky Way (Licquia & Newman 2015), and a metallicity of $1.58\,Z_\odot$. To demonstrate the potential dispersion in this relation, at a fixed redshift we plot the dispersion in slopes and growth/destruction rates using galaxies whose stellar masses are within 0.3 dex of the progenitor at that redshift. For the redshift evolution of the extinction law slope, we show the observed Milky Way range (Cardelli et al. 1989) with the light grey horizontal shaded region.

At early times while the metallicities are sufficiently low (redshift $z \gtrsim 2$), the masses of small grains double faster than the large grains, owing to their larger surface areas to volume ratios, and the extinction curves become rather steep. As the galaxy enriches the ISM with metals, however, the metallicity-dependent grain growth rates (c.f. equation 7) become sufficiently large to suppress the fraction of small grains, driving the small to large ratio (STL) down. This increase in the relative fraction of large to small grains flattens the extinction law slopes to within the observed range of slopes.

At the same time, the bump strengths depend primarily on the graphite to total dust mass ratio (hereafter graphite fraction). At early times, the silicates dominate as the dominant source of grain production is Type II SNe, the ejactae of which have relatively high non-carbon abundances. As AGB production becomes important, the graphite fraction increases due to its high carbon yield, and fluctuates around a certain value ($\sim$0.3) as the star formation activity stabilizes due to the regulation of feedback (and hence, the bump strength does as well). The variations of the graphite fraction is driven by the stochastic nature of the AGB metal enrichment versus

SN enrichment, as these two sources determine both the initial abundances of dust grains and metal abundances available for grain growth. Stochastic variations in the graphite fraction at late times drive similar variations in the bump strength. We now return to the bump-slope relation in Fig. 4. The variation in bump strengths at a fixed slope for our Milky Way analogues is due to variations in the graphite-to-silicate ratio at $z = 0$. That there is any sense of a bump-slope relation in observations along Galactic sightlines likely reflects relatively constant graphite-to-silicate ratios within the Milky Way.

4 DISCUSSION

4.1 Comparison to other numerical models

While we reviewed the current status of the theoretical literature in this field in Section 1, we remark briefly on numerical studies that specifically aim to understand the extinction law in Milky Way-like galaxies here.

Hou et al. (2019) adopted the 2-size model of Hirashita (2015) in order to investigate Milky Way extinction curves in cosmological simulations. Hou et al.'s simulation shows that the steepening of the extinction curves from $0.01 < Z/Z_\odot < 0.2$ due to accretion and the flattening from $Z/Z_\odot > 0.2$ due to enhanced coagulation. In our simulation, this is mainly caused by the non-monotonic effect of grain growth processes on small-to-large grain mass ratios when the sources for the production of small grains are limited. This discrepancy mainly comes from the different treatment of grain growth and feedback. Grain growth in our simulation is overall stronger. For example, considering gas with $(a/\mu\mathrm{m}, n_\mathrm{H}/\mathrm{cm}^{-3}, T_\mathrm{g}/\mathrm{K}, Z_\mathrm{g}) = (0.1, 100, 20, Z_\odot)$, the characteristic time-scale for grain growth is 4×10^7 yr in this work while $\sim 1 \times 10^8$ yr in their work. The difference may additionally owe to either the approximation of the continuous grain size distribution into two size bins by Hou et al., or alternatively to more subtle details of the subgrid treatment SIMBA galaxy formation physics that we employ as pointed out in Section 2.6.

A more recent work employing similar methods has been performed by Huang et al. (2021), who tracked a full spectrum of grain sizes in post-processed Illustris TNG model galaxies, though projected the galaxies into single zone models for computational efficiency. Their results show a good match with an MRN grain size distribution at $z \sim 1$, though the extinction curves of the same Milky Way analogues grow steeper than the observed Galactic curve at lower redshifts (i.e. towards $z \sim 0$). Huang et al. argue that this is due to a slight drop of both galaxy metallicities and dense gas fractions (which is not observed in our simulations) that lead to reduced coagulation rates. It is also possible that grain growth processes, which we find to be important for setting the grain size distribution in our simulations, are not as effective as in our model. Using one-zone models and fractions of dense gas computed by their equation (2) to limit the growth rates could potentially lead to the underestimation of grain growth in star-forming dense regions where most dust mass exists.

In an alternative class of models, McKinnon et al. (2018) and Aoyama et al. (2020) have developed on-the-fly models for a full spectrum of grain sizes in hydrodynamic simulations, as we have done here, though implemented these in idealized galaxy evolution models (i.e. those without a cosmological context). McKinnon et al. (2018) simulated the dust evolution in a Milky Way-mass disc galaxy in the absence of feedback, and indeed pioneered many of the equations and methods used in algorithms such as ours. McKinnon et al. found extinction curves that were steeper than that of the Galaxy. The overall effect of shattering on producing small grains in the McKinnon et al. model could be too strong due to the lack of feedback that could enhance the destructive processes of dust and possibly their computation of grain velocities leading to a high relative speed of colliding grains. Aoyama et al. (2020) clarified the importance of resolution of the simulations, and showed the different grain size distributions and importantly developed physical insight as to how grain size distributions vary as a function of the physical properties of the ambient ISM.

4.2 Generalization of model predictions and caveats

As we discussed in Section 1, the observed extinction laws in the Magellanic clouds vary such that the mean curve of the LMC is steeper than that of the Galaxy, with reduced bump strength, and the SMC is steeper yet with no or very small UV bump. This trend may be understandable from our simulations.

As is shown in Fig. 5, our model predicts an overall anticorrelation between metallicities Z and UV/optical slopes S for galaxies at $z < 2.5$, and the scatter is particularly tight at $Z > \sim 0.3 Z_\odot$. This trend is consistent with the fact that the Small Magellanic Cloud (SMC) and Large Magellanic Cloud (LMC) with average metallicities ~ 0.2 and $\sim 0.5\,Z_\odot$, respectively, tend to have steeper extinction curves than the Milky Way's (Russell & Dopita 1992). This said, while we achieve extinction laws with a wide range of bump strengths and slopes (c.f. Fig. 4), at metallicities comparable to the SMC and LMC, the vast majority of our simulated extinction curves have bump strengths larger than those observed in the Magellanic clouds. This owes primarily to the fact that the bump strengths are dominated by the graphite-to-silicate ratio, which does not evolve as fast with metallicity as the STL ratio does.

The lack of ability for our simulation to reproduce the location of the SMC in bump-slope space may represent an uncertainty in our simulation methods, i.e. an oversimplification when treating different grain species. Dust is assumed to be a mixture of graphite and silicate grains, but we do not evolve their grain size distribution separately, and omit the specific processes that may impact the lifecycle of 2175 Å bump carriers (including UV-photon processing). Beyond this, grain physics outside the scope of our current algorithms may contribute to the bump strength. For example, small PAHs with sizes $a < 0.001\mu$m may be associated with the UV bump (e.g. Mathis 1994; Dwek et al. 1997; Li & Draine 2001; Weingartner & Draine 2001; Siebenmorgen, Voshchinnikov & Bagnulo 2014). Other models in the carbonaceous-silicate family include e.g amorphous carbons (Zubko et al. 2004; Galliano et al. 2011) to replace non-PAH carbonaceous grains may help explain the bumpless feature in SMC environment (see Hirashita & Murga 2020), provided that a detailed treatment specifically for the production and destruction of 2175 Å bump carriers (e.g. PAH) is included. Inclusion of the detailed treatment of multiple grain species will be a major future direction of our work in order to capture the full features of the extinction curves.

5 CONCLUSIONS

The main focus of this paper has been to understand the origin of, and variation in dust extinction curves in Milky Way-mass galaxies at $z \sim 0$. To do this, we have developed a self-consistent model for evolving a distribution of dust grain sizes in cosmological hydrodynamic galaxy formation simulations that includes physical processes for dust formation in evolved stars, growth by the accretion of metals and coagulation, and destruction by thermal sputtering, grain shattering, and astration in star-forming regions. We have confirmed that these

models pass the benchmark of reproducing observed dust-to-gas ratio versus metallicity relations (Fig. 1). Our main results follow:

(i) Galaxies in our cosmological simulation with masses comparable to the Milky Way's exhibit a diverse range of modelled extinction laws, though they are all broadly within the range of curves observed within the Galaxy (Fig. 3 and Section 3.1). This broadly owes to modelled grain size distributions that converge to an MRN distribution at $z \sim 0$ in our simulations (Fig. 2).

(ii) As Milky Way progenitors evolve from high redshift towards $z = 0$, their extinction law slopes become flatter (to eventually be within the observed range of the Galaxy). This owes to an increase in the ratio of the grain growth to destruction rates, which is a consequence of increased galaxy ISM metal densities at late times (Fig. 6 and Section 3.2).

(iii) The bump strength is most closely dependent on the graphite-to-silicate ratio, which does not vary as strongly with the metallicity as the extinction law slope does. At $z = 0$, our model Milky Way analogues display both bump strengths and slopes comparable to the Milky Way (Fig. 4), though do not demonstrate any clear relationship between the two owing to fluctuations in the graphite-to-silicate ratio (Fig. 6). Whether a bona fide bump slope relationship in extinction laws exists is unclear from our simulations.

(iv) The increased extinction law slopes in our models at low metallicities may provide a natural explanation for the increased slopes in the LMC and SMC. This said, because our model evolves the grain size distribution for graphites and silicates simultaneously, we are not able to reproduce the bumpless curves of the SMC on average (though some individual models do indeed exhibit similar bumpless and steep curves). Future models that include models for evolving grain compositions are in progress.

ACKNOWLEDGEMENTS

QL was funded by a graduate fellowship from the University of Florida Informatics Institute, as well as NSF AST-1909153. The authors thank Hiroyuki Hirashita, Ryan McKinnon, Gergö Popping, Samir Salim, Karin Sandstrom and J. D. Smith for helpful conversations.

DATA AVAILABILITY

The data related to this publication will be shared on reasonable request to the corresponding author.

REFERENCES

Anglés-Alcázar D., Davé R., Faucher-Giguère C.-A., Özel F., Hopkins P. F., 2017a, MNRAS, 464, 2840
Anglés-Alcázar D., Faucher-Giguère C.-A., Kereš D., Hopkins P. F., Quataert E., Murray N., 2017b, MNRAS, 470, 4698
Aoyama S., Hou K.-C., Hirashita H., Nagamine K., Shimizu I., 2018, MNRAS, 478, 4905
Aoyama S., Hirashita H., Nagamine K., 2020, MNRAS, 491, 3844
Asano R. S., Takeuchi T. T., Hirashita H., Inoue A. K., 2013a, Earth Planets Space, 65, 213
Asano R. S., Takeuchi T. T., Hirashita H., Nozawa T., 2013b, MNRAS, 432, 637
Asplund M., Grevesse N., Sauval A. J., Scott P., 2009, ARA&A, 47, 481
Barlow M. J., 1978, MNRAS, 183, 367
Berry M. et al., 2012, ApJ, 757, 166
Bianchi S., Schneider R., 2007, MNRAS, 378, 973
Boylan-Kolchin M., Bullock J. S., Sohn S. T., Besla G., van der Marel R. P., 2013, ApJ, 768, 140
Cardelli J. A., Clayton G. C., Mathis J. S., 1989, ApJ, 345, 245
Clayton G. C., Martin P. G., 1985, ApJ, 288, 558
Clayton G. C., Gordon K. D., Wolff M. J., 2000, ApJS, 129, 147
Davé R., Thompson R., Hopkins P. F., 2016, MNRAS, 462, 3265
Davé R., Anglés-Alcázar D., Narayanan D., Li Q., Rafieferantsoa M. H., Appleby S., 2019, MNRAS, 486, 2827
De Vis P. et al., 2019, A&A, 623, A5
Dong H. et al., 2014, ApJ, 785, 136
Draine B. T., 2003, ApJ, 598, 1017
Draine B. T., Lee H. M., 1984, ApJ, 285, 89
Draine B. T., Salpeter E. E., 1979, ApJ, 231, 77
Dwek E., 1998, ApJ, 501, 643
Dwek E., 2016, ApJ, 825, 136
Dwek E., Scalo J. M., 1980, ApJ, 239, 193
Dwek E. et al., 1997, ApJ, 475, 565
Epstein P. S., 1924, Phys. Rev., 23, 710
Ferrarotti A. S., Gail H. P., 2006, A&A, 447, 553
Fitzpatrick E. L., 1985, ApJ, 299, 219
Fitzpatrick E. L., 1999, PASP, 111, 63
Fitzpatrick E. L., Massa D., 1986, ApJ, 307, 286
Fitzpatrick E. L., Massa D., 1988, ApJ, 328, 734
Fitzpatrick E. L., Massa D., 1990, ApJS, 72, 163
Fitzpatrick E. L., Massa D., 2007, ApJ, 663, 320
Fitzpatrick E. L., Massa D., 2009, ApJ, 699, 1209
Galliano F. et al., 2011, A&A, 536, A88
Galliano F., Galametz M., Jones A. P., 2018, ARA&A, 56, 673
Gioannini L., Matteucci F., Vladilo G., Calura F., 2017, MNRAS, 464, 985
Gjergo E., Granato G. L., Murante G., Ragone-Figueroa C., Tornatore L., Borgani S., 2018, MNRAS, 479, 2588
Gordon K. D., Clayton G. C., 1998, ApJ, 500, 816
Gordon K. D., Clayton G. C., Misselt K. A., Land olt A. U., Wolff M. J., 2003, ApJ, 594, 279
Granato G. L. et al., 2021, MNRAS, 503, 511
Hirashita H., 2000, PASJ, 52, 585
Hirashita H., 2015, MNRAS, 447, 2937
Hirashita H., Aoyama S., 2019, MNRAS, 482, 2555
Hirashita H., Murga M. S., 2020, MNRAS, 492, 3779
Hirashita H., Yan H., 2009, MNRAS, 394, 1061
Holwerda B. W., Keel W. C., Williams B., Dalcanton J. J., de Jong R. S., 2009, AJ, 137, 3000
Hopkins P. F., 2015, MNRAS, 450, 53
Hopkins P. F., Lee H., 2016, MNRAS, 456, 4174
Hopkins P. F., Kereš D., Oñorbe J., Faucher-Giguère C.-A., Quataert E., Murray N., Bullock J. S., 2014, MNRAS, 445, 581
Hopkins P. F. et al., 2018, MNRAS, 480, 800
Hou K.-C., Aoyama S., Hirashita H., Nagamine K., Shimizu I., 2019, MNRAS, 485, 1727
Huang Y.-H., Hirashita H., Hsu Y.-H., Lin Y.-T., Nelson D., Cooper A. P., 2021, MNRAS, 501, 1336
Iwamoto K., Brachwitz F., Nomoto K., Kishimoto N., Umeda H., Hix W. R., Thielemann F.-K., 1999, ApJS, 125, 439
Jones A. P., Duley W. W., Williams D. A., 1990, Q. J. R. Astron. Soc., 31, 567
Jones A. P., Tielens A. G. G. M., Hollenbach D. J., 1996, ApJ, 469, 740
Jones A. P., Köhler M., Ysard N., Bocchio M., Verstraete L., 2017, A&A, 602, A46
Kennicutt R. C., Jr, 1998, ApJ, 498, 541
Kim S.-H., Martin P. G., Hendry P. D., 1994, ApJ, 422, 164
Krumholz M. R., McKee C. F., Tumlinson J., 2009, ApJ, 699, 850
Laor A., Draine B. T., 1993, ApJ, 402, 441
Li A., Draine B. T., 2001, ApJ, 554, 778
Li A., Greenberg J. M., 1997, A&A, 323, 566
Li Q., Narayanan D., Davé R., 2019, MNRAS, 490, 1425
Licquia T. C., Newman J. A., 2015, ApJ, 806, 96
Mathis J. S., 1994, ApJ, 422, 176
Mathis J. S., Rumpl W., Nordsieck K. H., 1977, ApJ, 217, 425

McKee C., 1989, in Allamandola L. J., Tielens A. G. G. M., eds, Proc. IAU Symp. 135, Interstellar Dust. Kluwer Academic Publishers, Amsterdam, p. 431
McKee C. F., Hollenbach D. J., Seab G. C., Tielens A. G. G. M., 1987, ApJ, 318, 674
McKinnon R., Torrey P., Vogelsberger M., 2016, MNRAS, 457, 3775
McKinnon R., Torrey P., Vogelsberger M., Hayward C. C., Marinacci F., 2017, MNRAS, 468, 1505
McKinnon R., Vogelsberger M., Torrey P., Marinacci F., Kannan R., 2018, MNRAS, 478, 2851
Muratov A. L., Kereš D., Faucher-Giguère C.-A., Hopkins P. F., Quataert E., Murray N., 2015, MNRAS, 454, 2691
Nataf D. M. et al., 2016, MNRAS, 456, 2692
Nomoto K., Tominaga N., Umeda H., Kobayashi C., Maeda K., 2006, Nucl. Phys. A, 777, 424
Nozawa T., Kozasa T., Habe A., 2006, ApJ, 648, 435
Nozawa T., Asano R. S., Hirashita H., Takeuchi T. T., 2015, MNRAS, 447, L16
Oppenheimer B. D., Davé R., 2006, MNRAS, 373, 1265
Peek J. E. G., Graves G. J., 2010, ApJ, 719, 415
Pei Y. C., 1992, ApJ, 395, 130
Planck Collaboration XIII 2016, A&A, 594, A13
Popping G., Somerville R. S., Galametz M., 2017, MNRAS, 471, 3152
Prevot M. L., Lequeux J., Maurice E., Prevot L., Rocca-Volmerange B., 1984, A&A, 132, 389
Rémy-Ruyer A. et al., 2014, A&A, 563, A31
Russell S. C., Dopita M. A., 1992, ApJ, 384, 508
Salim S., Narayanan D., 2020, ARA&A, 58, 529
Schlafly E. F., Finkbeiner D. P., 2011, ApJ, 737, 103
Schlafly E. F. et al., 2010, ApJ, 725, 1175
Schlafly E. F. et al., 2014, ApJ, 789, 15
Schlafly E. F. et al., 2016, ApJ, 821, 78
Seab C. G., Shull J. M., 1983, ApJ, 275, 652
Siebenmorgen R., Kruegel E., 1992, A&A, 259, 614
Siebenmorgen R., Voshchinnikov N. V., Bagnulo S., 2014, A&A, 561, A82
Smith B. D. et al., 2017, MNRAS, 466, 2217
Solomon P. M., Rivolo A. R., Barrett J., Yahil A., 1987, ApJ, 319, 730
Somerville R. S., Davé R., 2015, ARA&A, 53, 51
Springel V., 2005, MNRAS, 364, 1105
Stebbins J., Huffer C. M., Whitford A. E., 1939, ApJ, 90, 209
Stecher T. P., Donn B., 1965, ApJ, 142, 1681
Stratta G., Maiolino R., Fiore F., D'Elia V., 2007, ApJ, 661, L9
Tielens A. G. G. M., McKee C. F., Seab C. G., Hollenbach D. J., 1994, ApJ, 431, 321
Tsai J. C., Mathews W. G., 1995, ApJ, 448, 84
Vijayan A. P., Clay S. J., Thomas P. A., Yates R. M., Wilkins S. M., Henriques B. M., 2019, MNRAS, 489, 4072
Vogelsberger M., McKinnon R., O'Neil S., Marinacci F., Torrey P., Kannan R., 2019, MNRAS, 487, 4870
Vogelsberger M., Marinacci F., Torrey P., Puchwein E., 2020, Nat. Rev. Phys., 2, 42
Wang S., Chen X., 2019, ApJ, 877, 116
Weingartner J. C., Draine B. T., 2001, ApJ, 563, 842
White Raymond E. I., Keel W. C., 1992, Nature, 359, 129
Yamasawa D., Habe A., Kozasa T., Nozawa T., Hirashita H., Umeda H., Nomoto K., 2011, ApJ, 735, 44
York D. G. et al., 2006, MNRAS, 367, 945
Zafar T., Watson D., Fynbo J. P. U., Malesani D., Jakobsson P., de Ugarte Postigo A., 2011, A&A, 532, A143
Zafar T. et al., 2018, MNRAS, 479, 1542
Zhukovska S., 2014, A&A, 562, A76
Zhukovska S., Dobbs C., Jenkins E. B., Klessen R. S., 2016, ApJ, 831, 147
Zubko V., Dwek E., Arendt R. G., 2004, ApJS, 152, 211

APPENDIX A: COMPUTING THE EXTINCTION CURVE

The optical depth at wavelength λ contributed by grains with radii a along a line of sight (LOS) is

$$\tau(a,\lambda)\mathrm{d}a = \int_{\mathrm{LOS}} \pi a^2 Q_{\mathrm{ext}}(a,\lambda) n_d(\mathbf{r},a)\mathrm{d}a\ \mathrm{d}s, \tag{A1}$$

where $n_d(\mathbf{r},a)\mathrm{d}a$ is the number density of grains with sizes $[a, a+\mathrm{d}a]$ at location $\mathbf{r}$. The extinction efficiency $Q_{\mathrm{ext}} = Q_{\mathrm{abs}} + Q_{\mathrm{sca}}$ is the ratio of extinction to geometric cross-section and considers effect of both absorption and scattering. Extinction efficiencies depend on the grain species (e.g. graphite or silicate in our simulation). Here we assume that the total carbon mass in the dust particles corresponds to the graphite mass, and the remainder goes to silicates. The extinction of dust grains is a summation of contributions from both graphite and silicate grains, weighted by their mass fractions. We adopt extinction efficiencies from Draine & Lee (1984) and Laor & Draine (1993), interpolating their results to grain sizes we are interested in.

We can then get the extinction

$$\begin{aligned} A(\lambda) &= 2.5\log_{10}(e)\int_{a_{\mathrm{min}}}^{a_{\mathrm{max}}} \tau(a,\lambda)\mathrm{d}a \\ &= 2.5\log_{10}(e)\int_{a_{\mathrm{min}}}^{a_{\mathrm{max}}} \mathrm{d}a\ \pi a^2 Q_{\mathrm{ext}}(a,\lambda)\int_{\mathrm{LOS}} n_d(\mathbf{r},a)\mathrm{d}s. \end{aligned} \tag{A2}$$

Considering the low resolution, we approximate $\int_{\mathrm{LOS}} n_d(\mathbf{r},a)\mathrm{d}s$ by $\overline{n_d(a)}\ L$, where $\overline{n_d(a)}$ is the average number density of grains over the entire galaxies, the extinction curve $A(\lambda)/A(V)$ versus $1/\lambda$ is therefore generated by

$$\left[\frac{A(\lambda)}{A(V)}\right] = \frac{\int_{a_{\mathrm{min}}}^{a_{\mathrm{max}}} a^2 Q_{\mathrm{ext}}(a,\lambda)\overline{n_d(a)}\ \mathrm{d}a}{\int_{a_{\mathrm{min}}}^{a_{\mathrm{max}}} a^2 Q_{\mathrm{ext}}(a,V)\overline{n_d(a)}\ \mathrm{d}a} \tag{A3}$$

This paper has been typeset from a TEX/LATEX file prepared by the author.